Successive switching among four states in a gain-loss-assisted optical microcavity hosting exceptional points up to order four

Arnab Laha [1,2] Dinesh Beniwal [3] and Somnath Ghosh [1,*]

[1]*Unconventional Photonics Laboratory, Department of Physics, Indian Institute of Technology Jodhpur, Rajasthan-342037, India*
[2]*Institute of Radiophysics and Electronics, University of Calcutta, Kolkata-700009, India*
[3]*Department of Physics, National Institute of Science Education and Research Bhubaneswar, Odisha 752050, India*

The implementation of exceptional points (EPs), a special type of topological singularities, has emerged as a new paradigm for engineering the quantum-inspired or wave-based photonic systems. Even though there exists a range of investigations on EPs of order two and three (say, EP2s and EP3s, respectively), the hosting of fourth-order EPs (EP4s) in any real system and the exploration of associated topological features are lacking. Here we have designed a simple Fabry-Pérot type gain-loss-assisted open optical microcavity to host EPs up to order four. The scattering-matrix formalism has been used to analyze the microcavity numerically. With the appropriate modulation of the gain-loss profile in the same cavity geometry, we have encountered multiple different orders of EPs by investigating the simultaneous interactions among four coupled cavity states via level-repulsion phenomena. Besides affirming the second-order and third-order branch-point behaviors of the embedded EP2s and EP3s, the fourth-order branch-point functionality of an EP4 has been manifested by encircling three connecting EP2s simultaneously in the closed gain-loss parameter space. We have established a unique successive state-switching phenomenon among four coupled states by implementing such an EP4-encirclement scheme in the system's parameter space. The proposed scheme indeed offers potential applications in state-switching and control in quantum-inspired integrated photonic circuits, where the presence of an EP4 serves as a new light manipulation tool.

I. INTRODUCTION

The promising interplay of topology and non-Hermiticity in an optical system has disclosed a new light manipulation tool by hosting exceptional points (EPs) that were once considered as purely mathematical [1–3]. EPs are a special kind of branch-point singularities, usually appearing in the parameter space of various non-Hermitian (open or nonconservative) systems. While a system encounters an EP, the coupled complex eigenvalues and the corresponding eigenstates simultaneously coalesce, and hence the eigenspace dimensionality of the underlying Hamiltonian is collapsed, referring to the EP as a topological defect [1–7]. Moreover, a parity-time ($\mathcal{PT}$) symmetric system, exhibiting real eigenvalues, undergoes a spontaneous phase transition from exact-$\mathcal{PT}$ phase to broken-$\mathcal{PT}$ phase at an EP [3]. The order of an EP is dictated by the number of coalescing states, i.e., an EP of order N (say, EPN) analytically connects N number of coupled eigenstates, where they coalesce simultaneously. However, $(N-1)$ number of EPs of order 2 (say, EP2) are also able to connect N number of coupled states analytically. It has been observed that the presence of $(N-1)$ EP2s in the system's parameter space performs a similar topological branch-point functionality of an EPN [8,9].

Over past two decades, extensive theoretical efforts have been put forward to explore the fundamental features of second- and third-order EPs (EP2s and EP3s, respectively) [5–15]. Moreover, exotic physical behaviors EP2s and EP3s have comprehensively been investigated in various open systems such as optical waveguide [16–23] and microcavity [24–27] arrangements, photonic crystals [28,29], laser systems [30–32], and also in some nonoptical systems, including atomic [33,34] and molecular [35] spectra, microwave systems [36–38], Bose-Einstein [39,40] and Bose-Hubbard [41] systems, and optomechanical cavities [42,43]. Especially in the optics and photonics domain, recent advanced technologies to implement EPs in various photonic systems with gain and loss have come up with a potential platform to meet a wide range of astonishing applications associated with the topological control of light-matter interactions [2] such as asymmetric mode conversion or switching [16,17,22,23], topological state flipping [24–27], control of lasing modes and antilasing [31,32], resonance tunneling [44], light amplification by parametric instability [45], unidirectional light propagation [46] including extremely enhanced nonreciprocal effects [47–49], stopping of light [50], and ultra-enhancement in optical sensing [51–54].

The presence of an EP2 is associated with the avoided resonance crossing (ARC) phenomenon around a square-root singularity between two coupled states with crossing or anti-crossing of their energies and widths (essentially, the real and imaginary parts of the corresponding eigenvalues) [5,22–25]. Now an EP3 can be encountered among three coupled states, where each of them individually interact with the other two states (keeping the third one as an observer) near two EP2s

---

in two different regimes of the system's parameter space. The presence of such two connecting EP2s holds the signature of the occurrence of a cube-root branch point, i.e., an EP3 in the same parameter space [8,14,15,26]. The branch-point behavior of the EPs can be established by encircling a particular EP with a stroboscopic simultaneous variation of coupling control parameters, which yields a successive state-transfer phenomenon among the corresponding coupled states [15, 22–26,38]. Here the coupled eigenvalues adiabatically exchange their positions, besides accumulating an additional Berry's phase by one of the associated eigenstates [38]. Now, if we consider time or length-scale dependent (dynamical) parametric variation around an EP, then the system's adiabatic behavior breaks down, enabling nonadiabatic dynamics of the coupled eigenstates with asymmetric population transfer [55,56]. Here one of the states that evolves with lower average loss behaves adiabatically and its coupled counterparts behave nonadiabatically. Such asymmetric state dynamics is associated with the chiral property of the underlying system, where irrespective of the inputs, the direction of the dynamical EP encirclement process decides the expected output [55]. The effect of such a parametric encirclement process around EP2s and EP3s and associated topological features have immensely been investigated in various configurations of optical microcavity [24–26] and waveguide [17,18,20–23] systems, and also verified experimentally [16,19].

Now it has been observed that the order of EPs plays a crucial role in the enhancement of the device performance. Beyond the current fundamental limits, the orders of magnitude enhancement of light-matter interactions can be achieved by hosting higher-order EPs. In this context the implementation of EP3s have attracted attention, owing to its cube-root response which is extremely sensitive to the external perturbation in comparison to the square-root response of an EP2 [51–53]. Thus it is expected that the fourth-root response to the perturbation due to hosting a fourth-order EP (EP4) can further enhance the performance of the underlying device. However, the hosting of EPs of the order of more than three and the corresponding analysis of the topological features are lacking. In this context, the topology of higher order EPs via emergence and coalescence of multiple EPs in a four-level system was experimentally investigated by using a coupled acoustic arrangement with asymmetric losses [57], and a similar approach of the interaction of multiple EPs induced by non-Hermitian coupling was numerically explored in a closed-form four-waveguide system [58]. A different approach of emergence and coalescence of multiple EPs has been reported by considering a periodically modulated $\mathcal{PT}$-symmetric quadrimer waveguide system, where the interactions of multiple EPs and their collision and mergence were induced by the periodic modulation, leading to Floquet higher-order EPs [59]. Such investigations dealt with a phase diagram featuring an exceptional point formation pattern (EPFP) to represent the occurrence of higher-order EPs. Beyond these few investigations, the direct observation of the fourth-order branch-point behavior of an EP4 was analytically established by considering a four-level Hamiltonian [60]. In contrast, implementing the branch-point behavior of an EP4, the realization of successive state exchange mechanisms among more than three states in any real photonic system

is yet to be explored. It was predicted that $(N^2 + N - 2)/2$ parameters are required to manipulate an EPN [9]. Beyond this prediction, a gain-loss-assisted microcavity system was explored to host an EP3 by varying only two tunable parameters [26]. However, the integration of higher-order EPs (of the order of more than three) demands a comparably complicated topology of the respective system. Thus from the application point of view, a potential platform to manipulate light can be explored by hosting different orders of EPs (up to order four) in the same passive optical system with a minimum number of tunable parameters. Thus, with a striking difference from the previously reported systems, in this work, a possibly simplest form of optical microcavity has been investigated to host EPs up to the order four.

In this paper we have reported a Fabry-Pérot type trilayer optical microcavity with a spatially unbalanced gain-loss profile to host EPs up to order four. The mutual coupling among four chosen cavity states have been investigated to encounter different orders of EPs by modulating the gain-loss profile based on only two tunable parameters. For the proposed microcavity configuration we have shown that only two control parameters, which is the minimum number of required parameters to manipulate an EP2, are sufficient to host up to fourth-order EPs. Here the scattering-matrix (*S*-matrix) formalism has been exploited to analyze the microcavity numerically. With the simultaneous variation of two chosen control parameters, at least three connecting EP2s have been identified among four coupled cavity states. Here multiple EP3s have been realized by enclosing different pairs of connecting EP2s inside the gain-loss parameter space. The second-order and third-order branch-point behaviors of the embedded EP2s and EP3s have been examined by considering adiabatic closed gain-loss variation around them. Now we have encountered an EP4 and presented a successive topological state conversion scheme among the four coupled states by considering an adiabatic encirclement scheme enclosing all the identified EP2s in the 2D gain-loss parameter plane. Such a unique microcavity configuration has been proposed to explore the topological features of EPs up to order four. The proposed scheme would indeed open up a state manipulation technique for state-of-the-art integrated devices.

II. FOUR-LEVEL STATE INTERACTION SCHEME: AN ANALYTICAL MODEL

Here we illustrate an interaction scheme among four coupled states using the framework of a four-level open system, which can be characterized by a 4×4 non-Hermitian Hamiltonian $\mathcal{H}$ having the form $H_0 + \lambda H_p$. Such a Hamiltonian has been written as

$$\mathcal{H} = [\varepsilon_j]^{4 \times 4}_{\text{diagonal}} + \lambda[\omega_{ij}]^{4 \times 4}_{\text{nondiagonal}}, \quad \{i, j\} \in \{1, 2, 3, 4\}.$$

$$(1)$$

The passive Hamiltonian H_0 represents a diagonal matrix with of four passive eigenvalues ε_j. The perturbation H_p represents a nondiagonal matrix having the elements ω_{ij} (i.e., $\omega_{ij} = 0$ for $i = j$). The parameter λ signifies the perturbation strength over H_p. Here we can conveniently introduce a tunable parameter, say η, to interconnect the coupling terms ω_{ij}, as $\omega_{ij} = \pm \eta \omega_{ji}$. Such a parameter dependent perturbation can

be analogous to optical gain-loss, while implementing a real system. Now the eigenvalue equation $|\mathcal{H}(\lambda) - EI| = 0$ (I represents a 4×4 identity matrix) gives a quartic equation of E, where the four corresponding roots, say E_j ($j = 1, 2, 3, 4$) express the four eigenvalues of $\mathcal{H}(\lambda)$.

Now, to describe the simultaneous interaction among four eigenvalues E_j ($j = 1, 2, 3, 4$) in the vicinity of a fourth-root branch point, we consider a specific point λ_c, where four eigenvalues are analytically connected. To ensure such analytical connection of E_j at $\lambda = \lambda_c$, the set of equations given below is to be simultaneously satisfied:

$$\frac{d^m}{dE^m} \det |\mathcal{H}(\lambda) - EI| = 0 \quad \text{with} \quad m = 0, 1, 2, 3. \quad (2)$$

Now, considering a critical eigenvalue E_c at $\lambda = \lambda_c$, the validity of Eq. (2) entitles the only possible form of E_j in terms of λ_c and E_c as

$$E_j(\lambda) = E_c + \sum_{u=1}^{\infty} a_u (\lambda - \lambda_c)^{u/4}. \quad (3)$$

Here a_u are some real constants. For distinguishing four eigenvalue levels (with $j = 1, 2, 3, 4$), Eq. (3) can be written more explicitly as

$$E_j(\lambda) = E_c + \sum_{u=1}^{\infty} a_u (\lambda - \lambda_c)^{u/4}$$
$$\times \exp\left[\frac{i \times u\{\arg(\lambda - \lambda_c) + 2\pi(j-1)\}}{4}\right]. \quad (4)$$

According to Eq. (4), four eigenvalue levels are defined by the quantity $(\lambda - \lambda_c)^{1/4}$ on first, second, third, and fourth Riemann surfaces in the λ plane. These four eigenvalue surfaces are connected through λ_c, where the associated fourth-root dependency of $E_j(\lambda)$, as can be seen in Eqs. (3) and (4), indicates the presence of a fourth-root branch point, i.e., an EP4. Now the structure of eigenfunctions in the presence of an EP4 can be written as

$$|\psi_j(\lambda)\rangle = |\psi_c\rangle + \sum_{u=1}^{\infty} (\lambda - \lambda_c)^{u/4} |\phi_u\rangle, \quad (5)$$

where the $|\psi_c\rangle$ has been considered as the critical eigenfunction at $\lambda = \lambda_c$. Now, considering the Riemann surfaces associated with E_j ($j = 1, 2, 3, 4$), the corresponding eigenfunctions can be written more explicitly as

$$|\psi_j(\lambda)\rangle = |\psi_c\rangle + \sum_{u=1}^{\infty} (\lambda - \lambda_c)^{u/4} |\phi_u^j\rangle \quad \text{with}$$
$$|\phi_u^j\rangle = \exp\left[\frac{i \times u\{\arg(\lambda - \lambda_c) + 2\pi(j-1)\}}{4}\right] |\phi_u\rangle. \quad (6)$$

Now, for all $\lambda \neq \lambda_c$, the possible pairs of eigenfunctions given by Eq. (6) form the usual biorthogonal complete system by validating the conditions

$$\langle \widetilde{\psi}_i(\lambda) | \psi_j(\lambda) \rangle = N_j(\lambda) \delta_{ij}, \quad (7a)$$

$$\sum_j \frac{|\psi_j(\lambda)\rangle \langle \widetilde{\psi}_j(\lambda)|}{\langle \widetilde{\psi}_j(\lambda) | \psi_j(\lambda) \rangle} = I. \quad (7b)$$

In Eq. (7), $\widetilde{\psi}$ and ψ represent the left and right eigenvectors. Now, considering the operation $\langle \widetilde{\psi}_i(\lambda) | \mathcal{H}(\lambda) - \mathcal{H}(\lambda_c) | \psi_j(\lambda) \rangle$, it can be shown that the scalar product given by Eq. (7a) vanishes as

$$N_j(\lambda) \sim p(\lambda - \lambda_c)^{3/4} \quad \text{for} \quad \lambda \to \lambda_c, \quad (8)$$

which reveals

$$\langle \widetilde{\psi}_i(\lambda) | \psi_c \rangle \sim q(\lambda - \lambda_c)^{3/4} \quad \text{for} \quad \lambda \to \lambda_c \quad (9)$$

after replacing one of the eigenvectors of the product [given on the left-hand side of Eq. (7a)] with $|\psi_c\rangle$. Here p and q are some constants. Thus, the consideration of $\lambda \to \lambda_c$ yields

$$\langle \widetilde{\psi}_c | \psi_c \rangle = 0 \quad \text{along with} \quad \langle \widetilde{\psi}_c | \phi_1 \rangle = 0 \quad (10)$$

even for $i \neq j$. $|\phi_1\rangle$ represents the first-order term in Eq. (3) corresponding to the first power of $(\lambda - \lambda_c)^{1/4}$. Equation (10) establishes analytic connection of four coupled states of $\mathcal{H}$ [given by Eq. (1)] in the vicinity of a fourth-root branch point, i.e., an EP4. Moreover, with appropriate settings of the coupling parameters, the presence of multiple EP2s and EP3s can be also be realized. In general, in the presence of an EP of order N, the eigenvalue levels are defined by the quantity $(\lambda - \lambda_c)^{1/N}$ on N number of Riemann surfaces in the λ plane.

Now we implement the above scenario by designing a simple fabrication feasible gain-loss-assisted optical microcavity, which can host EPs up to order four. Accordingly, as a four-level passive system (analogous to H_0), we have to choose four passive cavity states within a certain frequency range, which would be coupled with the onset of perturbation in terms of an unbalanced gain-loss profile (analogous to H_p). Here the gain-loss can be modulated with an appropriate choice of two tunable parameters (analogous to λ and η), which can control the overall interaction mechanism among the chosen cavity states.

III. DESIGN OF A FABRY-PÉROT TYPE OPTICAL MICROCAVITY

A. Cavity configuration with the operating parameters

We design a 1D Fabry-Pérot type trilayer open optical microcavity of length $L = 12$ μm, where a layer of high refractive indexed (say, n_c) material of the width of 9 μm has been sandwiched between two thin layers of the same low refractive indexed (say, n_g) materials of the width of 1.5 μm each. Here we choose $n_c = 2.65$ and $n_g = 1.5$. Figure 1(a) represents a schematic diagram of the microcavity. Beyond the $\mathcal{PT}$-symmetric constraints, the cavity has partially been pumped by integrating non-Hermiticity in terms of optical gain-loss (which is considered as the imaginary part of the refractive index). An unbalanced bilayer gain-loss profile has been introduced in both thin low-indexed regions, whereas in the intermediate high-indexed layer there is no gain-loss. The introduced gain-loss profile has been characterized by two tunable control parameters: gain coefficient (say, γ) and fractional loss-to-gain ratio (say, τ). Along the length scale of the microcavity, the overall nonuniform distribution of the complex refractive index profile within $0 \leqslant x \leqslant L$ (total
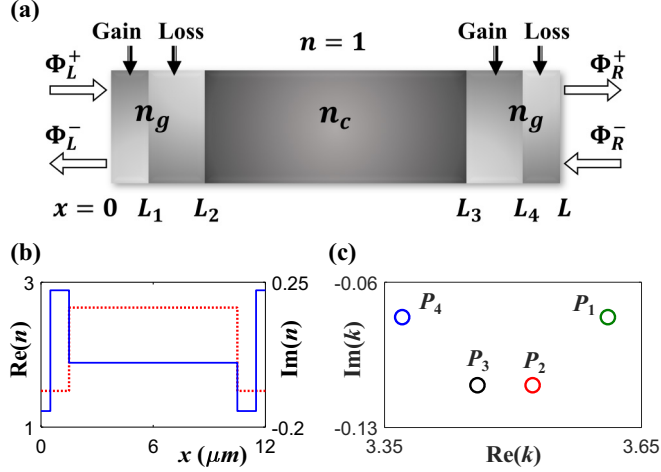
(a)

(b) **(c)**

FIG. 1. (a) Schematic diagram of the proposed trilayer optical microcavity, occupying the region $0 \leqslant x \leqslant L$ with $n_g = 1.5$, $n_c = 2.65$, $L = 12$ μm, $L_1 = 0.5$ μm, $L_2 = 1.5$ μm, $L_3 = 10.5$ μm, and $L_4 = 11.5$ μm. $\{\Phi_L^+, \Phi_R^-\}$ represents the set of incident waves from both sides, whereas $\{\Phi_L^-, \Phi_R^+\}$ represents the set scattered waves. (b) Complex refractive index profile [as given in Eq. (11)] along x direction, where the dotted red line represents the Re$[n(x)]$ (associated with the left y axis) and the solid blue line represents the [Im$n(x)$] (associated with the right y axis). (c) Initial positions of four chosen poles, say, P_1, P_2, P_3, and P_4 within the chosen frequency (k) range [3.35, 3.65] (in μm^{-1}).

length) can be written as

$$
n(x) = \begin{cases} n_g - i\gamma & : 0 \leqslant x \leqslant L_1 \text{ and } L_3 \leqslant x \leqslant L_4, \\ n_g + i\tau\gamma & : L_1 \leqslant x \leqslant L_2 \text{ and } L_4 \leqslant x \leqslant L, \\ n_c & : L_2 \leqslant x \leqslant L_3, \\ 1 & : \text{otherwise.} \end{cases}
$$

(11)

with $L_1 = 0.5$ μm, $L_2 = 1.5$ μm, $L_3 = 10.5$ μm, and $L_4 = 11.5$ μm. The complex profile of $n(x)$ has been shown in Fig. 1(b), where the dotted red and solid blue lines represent Re(n) (corresponding to the left y axis) and Im(n) (corresponding to the right y axis), respectively. A similar scalable prototype microcavity can be realized with a combination of glass-based materials with silicon carbide (SiC) based materials, where the customized gain-loss profile can be integrated via a controlled nonuniform pumping scheme or by doping of lossy and gain elements using a standard lithography technique.

B. Scattering matrix formalism: Calculation of cavity states

We adopt the scattering matrix (S-matrix) formalism method [61] to calculate the cavity states numerically. In this method the resonance states of the a real system are calculated in terms of the poles of the associated S matrix. Using the electromagnetic scattering theory, a 2×2 S matrix can be constructed to relate the input and output fields of the proposed 1D microcavity followed by $[\Phi_{\text{output}}] = [S][\Phi_{\text{input}}]$. Now if we consider $\{\Phi_L^+, \Phi_R^-\}$ and $\{\Phi_L^-, \Phi_R^+\}$ are the incident and scattered waves from both sides of the microcavity, as shown in Fig. 1(a), then the S-matrix equation can be

written as

$$
\begin{bmatrix} \Phi_{L0}^- \\ \Phi_{R0}^+ \end{bmatrix} = [S\{n(x), k\}] \begin{bmatrix} \Phi_{L0}^+ \\ \Phi_{R0}^- \end{bmatrix},
$$

(12)

where $\{\Phi_{L0}^+, \Phi_{R0}^-\}$ and $\{\Phi_{L0}^-, \Phi_{R0}^+\}$ represent the associated amplitudes. The matrix elements have been calculated as a function of cavity parameters and frequency (k). The poles of the defined S matrix has been calculated by solving

$$
\frac{1}{\max \left| \text{eig}[S\{n(x), k\}] \right|} = 0.
$$

(13)

We use numerical root finding method to solve Eq. (13).

To obey the conservation and causality conditions, only the solutions (poles) of Eq. (13), which appeared in the fourth quadrant of the complex k plane, are physically acceptable to represent the resonance states of the designed microcavity. In the passive cavity, the Re(k) of the poles of the associated S matrix can be calculated as Re(k) $= m\pi /n_R(x)L$ (with $m = 0, 1, 2, \ldots$), where m defines the order of the poles and $n_R(x)$ is the real part of $n(x)$ [62]. Now, investigating the ARC type interactions among the distributed poles over a wide k range with the onset of pumping (gain-loss), we judiciously choose four particular poles within a specific k range [3.35, 3.65] (in μm^{-1}). The circular markers of different colors in Fig. 1(c) show the initial positions of four chosen poles in the complex k plane. In the presence of gain-loss, the nonlinear initial distribution of P_j ($j = 1, 2, 3, 4$), as can be seen in Fig. 1(c), enables the mutual coupling among them with one-to-many coupling restrictions. Such nonlinear distribution of S-matrix poles can entirely be controlled by the choice of nonuniform $n_R(x)$ [24].

IV. RESULTS AND DISCUSSION

A. ARCs among the chosen poles: Toward encounter of multiple EP2s

The mutual interactions among the chosen poles P_j ($j = 1, 2, 3, 4$) with the introduction of gain-loss have been investigated via special avoided resonance crossing (ARC) phenomena by tuning two coupling control parameters γ and τ within a judiciously chosen interaction regime. While varying γ within $0 \leqslant \gamma \leqslant 0.5$, the trajectories of P_j in the complex k plane for different choices of τ have been shown in Fig. 2. The trajectories of P_j have been shown by dotted green, red, black, and blue curves for $j = 1, 2, 3$, and 4, respectively (such color variations are maintained throughout the paper for representing all the results). While investigating the trajectories of the chosen poles for different τ values, we observe that P_2 and P_3 interact strongly and approach an ARC near $\tau = 0.62$, where P_1 and P_4 behave as observers. Two different types of ARCs between P_2 and P_3 along with the presence of an EP2 have been shown in Fig. 2(a). For $\tau = 0.0622$, P_2 and P_3 exhibit an ARC with the increasing γ followed by an anticrossing in Re(k) with a simultaneous crossing in Im(k), as shown in Figs. 2(a.1) and 2(a.2), respectively. Now, while setting a slightly higher value of τ such as $\tau = 0.623$, P_2 and P_3 exhibit a different kind of ARC with the increasing γ, where we observe an exactly opposite behavior of Re(k) and Im(k). Here Re(k) of P_2 and P_3 undergo

P_1 .... P_2 .... P_3 .... P_4
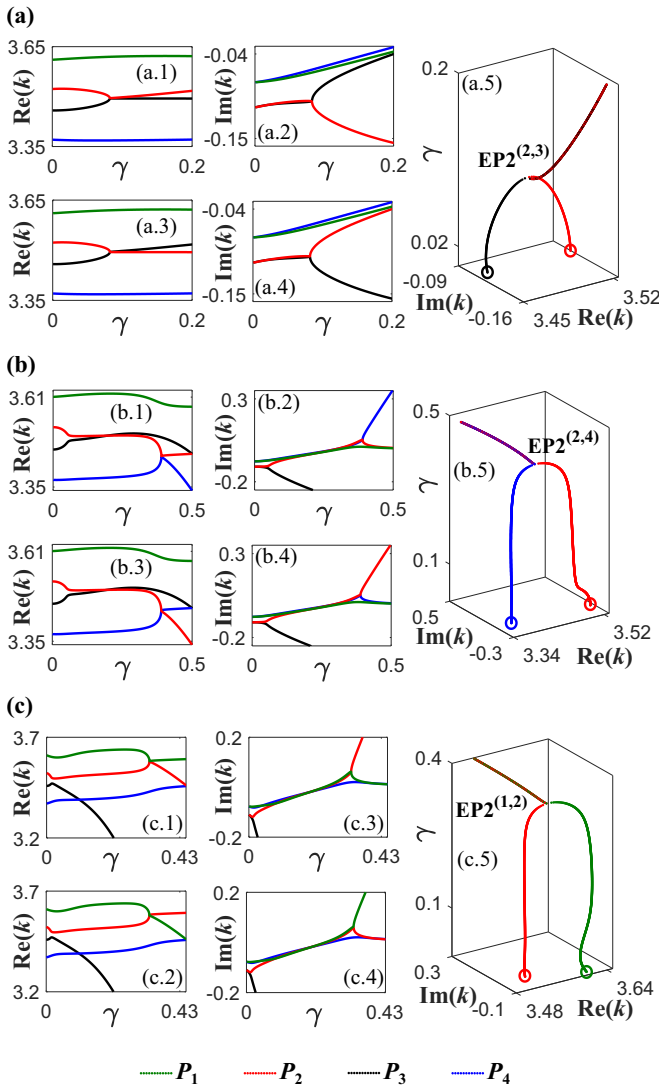
FIG. 2. Trajectories of Re(k) and Im(k) associated with P_j ($j = 1, 2, 3, 4$) for different τ values, while varying γ within [0, 0.5]. Here the dotted green, red, black, and blue curves represent the trajectories of P_1, P_2, P_3, and P_4, respectively. (a) P_2 and P_3 exhibit ARC (unaffecting P_1 and P_4) with (a.1) an anticrossing in Re(k) and (a.2) a simultaneous crossing in Im(k) for $\tau = 0.622$, and (a.3) a crossing in Re(k) and (a.4) a simultaneous anticrossing in Im(k) for $\tau = 0.623$; (a.5) P_2 and P_3 coalesce at $\gamma \approx 0.083$ for $\tau = 0.6288$, referring to the encounter of EP2$^{(2,3)}$. (b) P_2 and P_4 exhibit ARC (unaffecting P_1 and P_3) with (b.1) an anticrossing in Re(k) and (b.2) a simultaneous crossing in Im(k) for $\tau = 0.8825$, and (b.3) a crossing in Re(k) and (b.4) a simultaneous anticrossing in Im(k) for $\tau = 0.883$; (b.5) P_2 and P_4 coalesce at $\gamma \approx 0.389$ for $\tau = 0.8827$, referring to the encounter of EP2$^{(2,4)}$. (c) P_1 and P_2 exhibit ARC (unaffecting P_3 and P_4) with (c.1) an anticrossing in Re(k) and (c.2) a simultaneous crossing in Im(k) for $\tau = 2.786$, and (c.3) a crossing in Re(k) and (c.4) a simultaneous anticrossing in Im(k) for $\tau = 2.787$; (c.5) P_1 and P_2 coalesce at $\gamma \approx 0.332$ for $\tau = 2.7866$, referring to the encounter of EP2$^{(1,2)}$. In (a.5), (b.5), and (c.5), only the trajectories of the coalescing states have been shown for a clear visualization. (The unit of k: μm^{-1}.)

a crossing, whereas the corresponding Im(k) experience a simultaneous crossing, as can be seen in Figs. 2(a.3) and 2(a.4),

respectively. However, it has been observed that for both τ values P_1 and P_4 remain away from the ARC regime of P_2 and P_3. Such two topologically dissimilar ARCs for two different τ values indicate the presence of an EP2 for an intermediate τ. In Fig. 2(a.5) we choose $\tau = 0.6228$, for which P_2 and P_3 coalesce near $\gamma \approx 0.083$, referring to the presence of an EP2, say EP2$^{(2,3)}$, at $\sim$(0.083, 0.6228) in the (γ, τ) plane.

In a similar way we further encounter two other EP2s associated with the pairs $\{P_2, P_4\}$ and $\{P_1, P_2\}$ at two different locations in the (γ, τ) plane. A strong level repulsion between P_2 and P_4 has been observed near $\tau = 0.88$, where P_1 and P_3 behave as observers. On the other hand, P_1 and P_2 interact strongly and approach ARC, keeping P_3 and P_4 as observers, near $\tau = 2.78$. The type of interactions between the poles from the pairs $\{P_2, P_4\}$ and $\{P_1, P_2\}$ for different τ values have been shown in Figs. 2(b) and 2(c), and also summarized in Table I (including the interactions for the pair $\{P_2, P_3\}$, as already described). Thus, only modulating two coupling control parameters γ and τ, we encounter three such cases, where three different pairs from four chosen poles interact around three connecting EP2s, keeping the rest as observers. The locations of three EP2s have also been given in Table I. Here the pole P_2 behaves as a common state and is allowed to interact with the rest of the three states via three identified EP2s. Within a chosen interaction regime, such a situation reveals the presence of higher-order EPs even up to order four (as there are three connecting EP2s), which connect all four chosen poles (cavity states) analytically.

Now the topological features associated with different orders of branch-point behaviors can be observed by encircling single or multiple EP2s in the system parameter space. To carry out an encirclement process in the system's parameter space, we consider the parametric equation:

$$\gamma(\alpha) = \gamma_0 \sin\left(\frac{\alpha}{2}\right) \quad \text{and} \quad \tau(\alpha) = \tau_0 + a \sin(\alpha), \quad (14)$$

which governs the simultaneous closed variations of γ and τ over the tunable angle $\alpha \in [0, 2\pi]$. (γ_0, τ_0) and a are the characteristics parameters, where γ_0 must be greater than the γ value associated with the respective EP2, which is to be encircled (for encircling multiple EP2s simultaneously, we have to consider comparably higher γ value). For $0 \leqslant \alpha \leqslant 2\pi$, $a > 0$ enables the clockwise parametric variation, whereas $a > 0$ enables the anticlockwise parametric variation along a specific loop. The choice of such a specific type of parametric equation allows us to consider a closed loop with $\gamma = 0$ at both the starting and end point, which would be suitable to track the dynamics of the chosen poles from their passive locations. This is indeed suitable for device implementation of the proposed scheme.

Here the second-order branch-point features can be explored by encircling each of the identified EP2s, individually in the (γ, τ) plane. Whereas the third-order branch-point behavior associated with an EP3 can be observed by enclosing two connecting EP2s (associated with three coupled states) inside the parametric loop. Here a maximum of three EP3s can be identified by simultaneously encircling different pairs among three EP2s. Furthermore, the simultaneous parametric encirclement enclosing all three connecting EP2s identified among four chosen poles can reveal the fourth-order

TABLE I. Interaction schemes associated with the pairs $\{P_2, P_3\}$, $\{P_2, P_4\}$, and $\{P_1, P_2\}$ for different τ values, while varying γ in between $[0, 0.5]$. The locations of three corresponding EP2s in the (γ, τ) plane are also given in this table.

Strongly interacting states exhibiting ARC	τ values	Type of interactions		Locations of EP2s		
		Re(k)	Im(k)	γ_{EP}	τ_{EP}	EP2
P_2 and P_3	0.622	Anticrossing [Fig. 2(a.1)]	Crossing [Fig. 2(a.2)]	0.083	0.6228	EP2$^{(2,3)}$
	0.623	Crossing [Fig. 2(a.3)]	Anticrossing [Fig. 2(a.4)]			
	0.6288	Coalescence [Fig. 2(a.5)]				
P_2 and P_4	0.8825	Anticrossing [Fig. 2(b.1)]	Crossing [Fig. 2(b.2)]	0.389	0.8827	EP2$^{(2,4)}$
	0.883	Crossing [Fig. 2(b.3)]	Anticrossing [Fig. 2(b.4)]			
	0.8827	Coalescence [Fig. 2(b.5)]				
P_1 and P_2	2.786	Anticrossing [Fig. 2(c.1)]	Crossing [Fig. 2(c.2)]	0.332	2.7866	EP2$^{(1,2)}$
	2.787	Crossing [Fig. 2(c.3)]	Anticrossing [Fig. 2(c.4)]			
	2.7866	Coalescence [Fig. 2(c.5)]				

branch-point feature, which has been explored by implementing any real optical system. With judicious choices of (γ_0, τ_0) and a, we can consider different encirclement processes to enclose single or multiple EP2s. Such parametric encirclement schemes can lead to different type of state-flipping applications, which has been explored in the following sections.

B. Encircling the EP2s individually in the system parameter space: Toward state flipping between two states

Here we study the effect of stroboscopic encirclement around individual EP2s in the system's parameter plane on the dynamics of four chosen poles in the complex k plane. To encircle each of the EP2s individually in the (γ, τ) plane, we consider three different parametric loops [following Eq. (14)], which have been shown in Fig. 3(a); where Loop-1, Loop-2, and Loop-3 individually encircles EP2$^{(1,2)}$, EP2$^{(2,3)}$,

and EP2$^{(2,4)}$, respectively. The characteristics parameters, i.e., γ_0, τ_0, and a, associated with these three loops have been given in Table II. Three crosses in Fig. 3(a) represent the locations of three EP2s. Here, to perform a particular encirclement process, the parameters γ and τ have been varied very slowly in the clockwise direction along a particular loop. In Figs. 3(b)–3(d) we show the trajectories of four coupled poles P_j ($j = 1, 2, 3, 4$) in the complex k plane following three separate parametric encirclement processes along Loop-1, Lopp-2, and Loop-3, respectively. Here the dotted green, red, black, and blue curves represents the evolutions P_j (for $j = 1, 2, 3$, and 4, respectively) from their passive locations (i.e., while initializing the encirclement process; the passive locations are highlighted by the circular markers of respective colors) in the complex k plane, following each point evolution along a particular loop in the (γ, τ) plane.
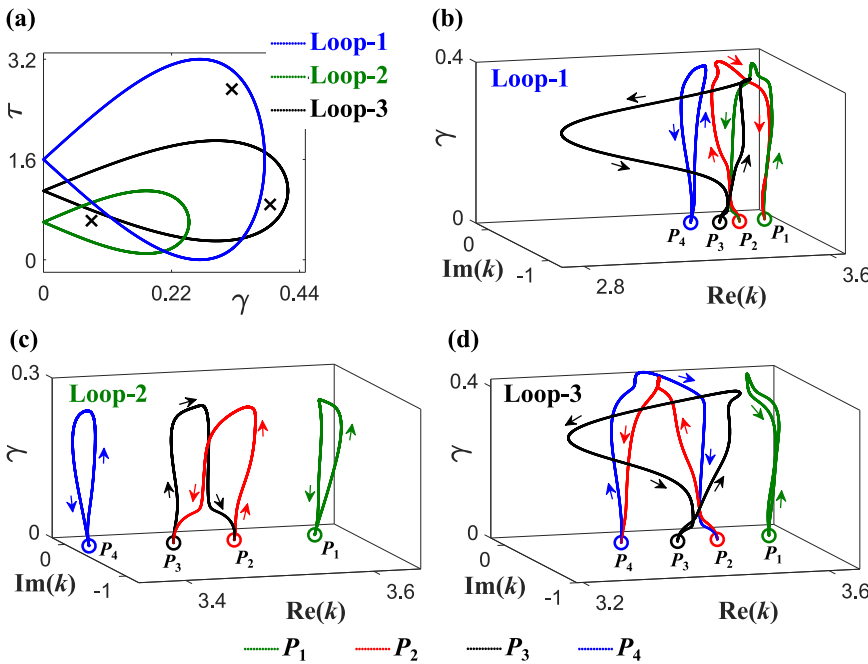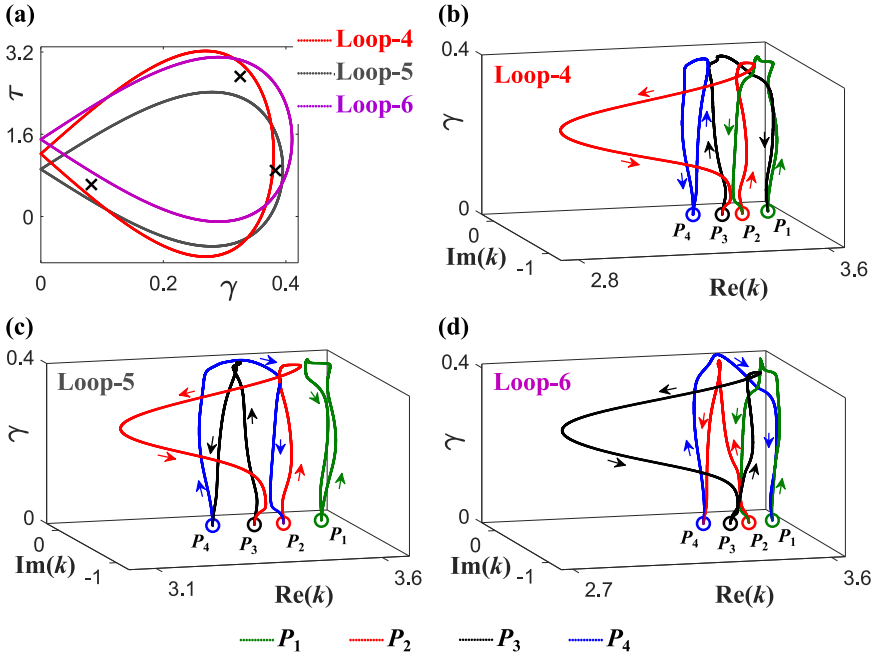

FIG. 3. (a) Three parametric loops in the (γ, τ) plane [following Eq. (14)] to encircle the identified EP2s individually, where Loop-1, Loop-2, and Loop-3 individually enclose EP2$^{(1,2)}$, EP2$^{(2,3)}$, and EP2$^{(2,4)}$, respectively. Here we consider the clockwise encirclement direction. Three crosses indicate the location of three EP2s. (b) The trajectories of P_j ($j = 1, 2, 3, 4$) following the parametric encirclement process along Loop-1, exhibiting an adiabatic state-flipping $P_1 \rightarrow P_2 \rightarrow P_1$, unaffecting $P_3 (\rightarrow P_3)$ and $P_4 (\rightarrow P_4)$. (c) Similar trajectories of P_j ($j = 1, 2, 3, 4$) following the parametric encirclement process along Loop-2, exhibiting an adiabatic state-flipping $P_2 \rightarrow P_3 \rightarrow P_2$, unaffecting $P_1 (\rightarrow P_1)$ and $P_4 (\rightarrow P_4)$. (d) Similar trajectories following the parametric encirclement process along Loop-3, exhibiting an adiabatic state-flipping $P_2 \rightarrow P_4 \rightarrow P_2$, unaffecting $P_1 (\rightarrow P_1)$ and $P_3 (\rightarrow P_3)$. In (b) and (c) the circular markers of respective colors indicate the passive locations of P_j, i.e., while initializing the encirclement from $\gamma = 0$. Arrows of respective colors indicate their progression directions. (The unit of k: μm^{-1}.)

(a)

(b)

(c)

(d)

FIG. 4. Three parametric loops in the (γ, τ) plane [following Eq. (14)], where each loop individually encloses at least two connecting EP2s among three identified EP2s. Here Loop-4, Loop-5, and Loop-6 individually enclose the pairs $\{EP2^{(1,2)}, EP2^{(2,3)}\}$, $\{EP2^{(2,3)}, EP2^{(2,4)}\}$, and $\{EP2^{(1,2)}, EP2^{(2,4)}\}$, respectively. (b) The trajectories of $P_j (j = 1, 2, 3, 4)$ following the clockwise parametric encirclement process along Loop-4, exhibiting an adiabatic successive state-switching process $P_1 \rightarrow P_2 \rightarrow P_3 \rightarrow P_1$, unaffecting $P_4 (\rightarrow P_4)$. (c) Similar trajectories of $P_j (j = 1, 2, 3, 4)$ following the parametric encirclement process along Loop-5, exhibiting an adiabatic successive state-switching process $P_2 \rightarrow P_3 \rightarrow P_4 \rightarrow P_2$, unaffecting $P_1 (\rightarrow P_1)$. (d) Similar trajectories following the parametric encirclement process along Loop-6, exhibiting an adiabatic successive state-switching process $P_1 \rightarrow P_2 \rightarrow P_4 \rightarrow P_1$, unaffecting $P_3 (\rightarrow P_3)$. The notations and colors bear the same meaning as we have already described in the caption of Fig. 3. (The unit of k: μm^{-1}.)

Now, following the encirclement process along Loop-1, which encircles only $EP2^{(1,2)}$, keeping $EP2^{(2,3)}$ and $EP2^{(2,4)}$ outside, we track the trajectories of four chosen poles in Fig. 3(b). Here it has been shown that only poles P_1 and P_2, which are analytically connected by $EP2^{(1,2)}$, are adiabatically swapping their initial positions with the closed variation of γ and τ along Loop-1, and perform a complete state-switching process in the complex k plane followed by $P_1 \rightarrow P_2 \rightarrow P_1$ with the completion of the encirclement process in the (γ, τ) plane. However, the encirclement process along Loop-1 does not affect P_3 and P_4. They follow two individual closed trajectories in the complex k plane and remain in the same states at the end of the encirclement process. Here the adiabatic state flipping between P_1 and P_2 confirms the second-order branch-point behavior of $EP2^{(1,2)}$. In a similar way, the second-order branch-point behaviors of $EP2^{(2,3)}$ and $EP2^{(2,4)}$ have been verified in Figs. 3(c) and 3(d). In Fig. 3(c), the trajectories of P_j have been shown for a complete parametric encirclement process along Loop-2, which encloses only $EP2^{(2,3)}$, whereas it keeps $EP2^{(1,2)}$ and $EP2^{(2,4)}$ outside. Accordingly, in the complex k plane, a complete adiabatic permutation between P_2 and P_3 has been observed following the sequence $P_2 \rightarrow P_3 \rightarrow P_2$, where P_1 and P_4 remain unaffected and make individual loops. Now, for a complete parametric cycle along Loop-3, which encloses only $EP2^{(2,4)}$ among three identified EP2s, the similar trajectories have been shown in Fig. 3(d). Such an encirclement process yields an adiabatic state flipping between P_2 and P_4 ($P_2 \rightarrow P_4 \rightarrow P_2$) in the complex k plane, unaffecting the trajectories of P_1 and P_3. Thus the individual encirclement process around each of the identified EP2s in (γ, τ) plane allows the adiabatic flipping between two associated coupled states in the complex k plane even in the presence of two nearby states. During the exhibition of the trajectories of P_j in the complex k plane, we additionally plot

the variation of γ along the z axis for clarity. Moreover, we use arrows of respective colors to highlight the trajectories of P_j.

C. Parametric encirclement schemes to enclose two EP2s simultaneously: Toward successive state switching among three states

Here we consider three pairs among three identified EP2s viz. $\{EP2^{(1,2)}, EP2^{(2,3)}\}$, $\{EP2^{(2,3)}, EP2^{(2,4)}\}$, and $\{EP2^{(1,2)}, EP2^{(2,4)}\}$, where the EP2s of each pair have been encircled simultaneously in the (γ, τ) plane. Accordingly, we consider such three parametric loops following Eq. (14), which have been shown in Fig. 4(a). Here Loop-4 encloses $EP2^{(1,2)}$ and $EP2^{(2,3)}$ simultaneously, whereas it keeps $EP2^{(2,4)}$ outside. Similarly, Loop-5 and Loop-6 have been considered to encircle only the EP2s from the pairs $\{EP2^{(2,3)}, EP2^{(2,4)}\}$ and $\{EP2^{(1,2)}, EP2^{(2,4)}\}$, respectively. The values of γ_0, τ_0, and a associated with these three loops have been given in Table II. The notation and colors bear the exact same meaning, as we have already discussed. Now, such an encirclement process around two connecting EP2s can lead the functionality of a cube-root branch point, i.e., an EP3. Now the trajectories of P_j following the encirclement processes along Loop-4, Loop-5, and Loop-6 have been shown in Figs. 4(b)–4(d).

In Fig. 4(b) we exhibit the trajectories of P_j following the stroboscopic parametric variation along Loop-4 (enclosing only $EP2^{(1,2)}$ and $EP2^{(2,3)}$). Here we observe that poles P_1, P_2, and P_3, which are analytically connected via two connecting EP2s (i.e., $EP2^{(1,2)}$ and $EP2^{(2,3)}$; encircled by Loop-4), are exchanging their identities. After completing the encirclement process in the (γ, τ) plane, they switch adiabatically in a successive manner $P_1 \rightarrow P_2 \rightarrow P_3 \rightarrow P_1$ in the complex k plane and make a complete loop. However, this

encirclement process does not affect E_4, which remain in the same state at the end of the encirclement process. Such a successive states switching phenomenon firmly reflects the third-order branch-point feature associated with the presence of an EP3 in the same parameter space, where P_1, P_2, and P_3 are analytically connected. Now, if we consider the parametric cycle along Loop-5 (enclosing only EP2$^{(2,3)}$ and EP2$^{(2,4)}$), then we observe a successive and adiabatic switching among the associated connected states P_2, P_3, and P_4 followed by $P_2 \rightarrow P_3 \rightarrow P_4 \rightarrow P_2$ in Fig. 4(c), where P_1 remains unaffected. Thus we can confirm the presence of another EP3 to connect P_2, P_3, and P_4. Similarly, the parametric variation along Loop-6 (enclosing only EP2$^{(1,2)}$ and EP2$^{(2,4)}$) results in the adiabatic switching $P_1 \rightarrow P_2 \rightarrow P_4 \rightarrow P_1$ in a successive manner, unaffecting P_3, as can be seen in Fig. 4(d), which reflects the presence of an EP3 to connect P_1, P_2, and P_4 analytically. Thus, we host three EP3s in the presence of three connecting EP2s among four coupled poles, where considering the stroboscopic encirclement process around the embedded EP3s, immutable successive state-switching applications among three associated states have been manifested even in the presence of a nearby fourth state.

D. Parametrically encircling three EP2s simultaneously: Toward successive state switching among four states

Now we perform a quasistatic parametric encirclement process to enclose three connecting EP2s simultaneously in the (γ, τ) plane and investigate the associated topology by tracing the trajectories of P_j ($j = 1, 2, 3, 4$) in the complex k plane. Figure 5 shows the corresponding results including the structure of Riemann surfaces within the interaction regime. With appropriate choice of γ_0, τ_0, and a (as given in Table II), we consider a suitable parametric loop, say Loop-7, following Eq. (14) to encircle all three connecting EP2s, i.e., EP2$^{(1,2)}$, EP2$^{(2,3)}$, and EP2$^{(2,4)}$, which have been shown by the brown loop in the inset of Fig. 5(a) (where three crosses represent the locations of three EP2s). Here the brown arrows represent the clockwise parametric variation along Loop-7. Here we explore that all the coupled poles P_j are exchanging their identities with the stroboscopic parametric variation along Loop-7. Interestingly, with the completion of this encirclement process, all the four consecutive chosen poles carry out a successive state switching process followed by $P_1 \rightarrow P_2 \rightarrow P_3 \rightarrow P_4 \rightarrow P_1$, adiabatically to make a complete loop in the k plane. Such a successive state switching process is evident from the trajectories shown in Fig. 5(a).

The formation of the Riemann surfaces corresponding to P_j ($j = 1, 2, 3, 4$) concerning the simultaneous variations of the coupling parameters γ and τ within the interaction regime have been shown in Fig. 5(b), where the distributions of Re(k) and Im(k) are exhibited separately in Figs. 5(b.1) and 5(b.1), respectively. The simultaneous interaction among the four chosen poles can easily be understood from the associated Riemann sheet distribution. The successive state transfer process following the parametric variation along Loop-7 has also been shown by mapping the trajectories of P_j on their respective Riemann surfaces. Here the successive switching phenomenon among the coupled poles P_j from their respective surfaces is clearly evident.
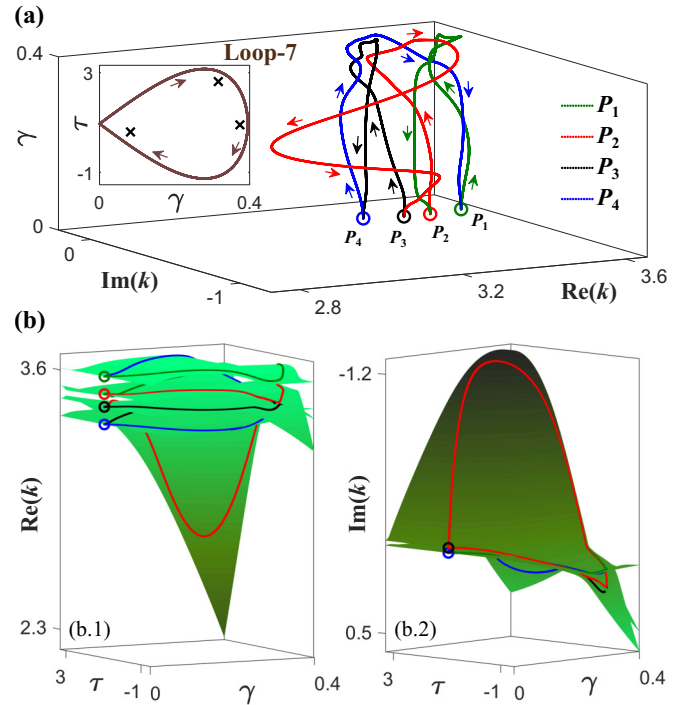

FIG. 5. (a) The trajectories of P_j ($j = 1, 2, 3, 4$) in the complex k plane, following a clockwise encirclement process along Loop-7 (as shown in the inset), which encloses all three identified EP2s (i.e., EP2$^{(1,2)}$, EP2$^{(2,3)}$, and EP2$^{(2,4)}$) simultaneously. Here they execute a successive state-switching process following the manner $P_1 \rightarrow P_2 \rightarrow P_3 \rightarrow P_4 \rightarrow P_1$ with the completion of the encirclement process. (b) The formation of the Riemann surfaces corresponding to P_j as a function of γ and τ with the overall variation of (b.1) Re(k) and (b.2) Im(k) within the interaction regime. The trajectories of P_j following the parametric encirclement process along Loop-7 have been mapped on their respective Riemann sheets for a clear understanding of the successive state transfer mechanism among four coupled poles from their corresponding surfaces. The notations and colors bear the same meaning as we have already described in the caption of Fig. 3. (The unit of k: μm^{-1}.)

Such unconventional topology of four coupled poles around their three connecting EP2s certainly conveys the fourth-order branch-point feature with the presence of a fourth-root singularity, i.e., an EP4 in the same parameter space. Here four complete encirclement process in a row along the same parametric loop is required to regain the initial locations of P_j. Such an EP4-aided topological state-switching process has also been examined for an anticlockwise parametric variation along Loop-7, where it has been observed that four coupled poles switch their identities following the manner $P_1 \rightarrow P_4 \rightarrow P_3 \rightarrow P_2 \rightarrow P_1$, which is opposite to the sequence, as can be seen for the clockwise parametric encirclement process.

Thus, using the same framework of a simple optical microcavity with an unbalanced gain-loss profile, we have investigated the hosting EPs up to order four and explored the successive state switching schemes up to among four coupled cavity states with an appropriate choice of a stroboscopic EP-encirclement process in the system's 2D parameter space. Without using any complex system with many controlling

TABLE II. The characteristics of all the chosen parametric loops (Loop-1–Loop-7), including the values of γ_0, τ_0, and a [following Eq. (14)] for each loop and the overall device performance in the context of topological state-switching applications.

Parametric loops	Characteristics parameters			EPs inside the loop	Topological state switching
	γ_0	τ_0	a		
Loop-1 [Fig. 3(a), blue curve]	0.38	1.6	1.6	EP2$^{(1,2)}$	$P_1 \rightarrow P_2 \rightarrow P_1$ $P_3 \rightarrow P_3$, $P_4 \rightarrow P_4$ [Fig. 3(b)]
Loop-2 [Fig. 3(a), green curve]	0.25	0.6	0.5	EP2$^{(2,3)}$	$P_2 \rightarrow P_3 \rightarrow P_2$ $P_1 \rightarrow P_1$, $P_4 \rightarrow P_4$ [Fig. 3(c)]
Loop-3 [Fig. 3(a), black curve]	0.42	1.1	0.8	EP2$^{(2,4)}$	$P_2 \rightarrow P_4 \rightarrow P_2$ $P_1 \rightarrow P_1$, $P_3 \rightarrow P_3$ [Fig. 3(c)]
Loop-4 [Fig. 4(a), red curve]	0.38	1.22	2	EP2$^{(1,2)}$ and EP2$^{(2,3)}$	$P_1 \rightarrow P_2 \rightarrow P_3 \rightarrow P_1$ $P_4 \rightarrow P_4$ [Fig. 4(b)]
Loop-5 [Fig. 4(a), gray curve]	0.395	0.92	1.5	EP2$^{(2,3)}$ and EP2$^{(2,4)}$	$P_2 \rightarrow P_3 \rightarrow P_4 \rightarrow P_2$ $P_1 \rightarrow P_1$ [Fig. 4(c)]
Loop-6 [Fig. 4(a), violet curve]	0.41	1.5	1.64	EP2$^{(1,2)}$ and EP2$^{(2,4)}$	$P_1 \rightarrow P_2 \rightarrow P_4 \rightarrow P_1$ $P_3 \rightarrow P_3$ [Fig. 4(d)]
Loop-7 [Fig. 5(a), inset]	0.395	0.95	2.2	EP2$^{(1,2)}$, EP2$^{(2,3)}$, and EP2$^{(2,4)}$	$P_1 \rightarrow P_2 \rightarrow P_3 \rightarrow P_4 \rightarrow P_1$ (Fig. 5)

parameters, we have considered only two tunable parameters associated with the gain-loss profile to host higher-order EPs. The overall device performance for all the chosen parametric loops have been summarized in Table II, where the branch-point features of EPs up to order four have been revealed.

In this context, if we consider the time dependence in the parametric variation during the encirclement of single or multiple EPs, then the breakdown of the adiabatic theorem in the system's dynamics can be observed [55,56], which has a direct implication on the time-asymmetric and nonadiabatic evolution of the coupled states. Such nonadiabatic state dynamics can be observed in any length-dependent guided-wave system hosting a dynamical EP encirclement scheme, where the time evolution of coupling control parameters can analogically be realized by mapping the parameter space along the length axis [16,17,20–23,49]. However, in the proposed 1D Fabry-Pérot type microcavity, we have computed the resonance states associated with the longitudinal modes by analyzing the S matrix, where there is no additional propagation axis. In this framework, the dynamical EP encirclement schemes to study the time or length-scale dependent model propagation are impossible to implement directly. Here the trajectories of cavity states in terms of S-matrix poles have straightforwardly been analyzed by considering various quasistatic encirclement processes in the cavity-parameter plane, for which only the adiabatic evolutions and the corresponding state-switching phenomenon are evident.

From our comprehensive investigation to reach the fourth-order branch-point behavior of an EP4 even with the simultaneous presence of multiple connecting EP2s and EP3s, it is evident that the proposed scheme of the hosting of a different order of EPs in a particular optical system certainly enhances the degrees of freedom to manipulate the states via light-matter interactions and indeed boost the device performance in the context of state-switching applications. The proposed scheme can also be implemented in any guided-wave systems to further investigate the nonadiabatic

correlations and corresponding chiral aspects associated with the dynamical (time dependent) encirclement process around an EP4. Such investigations indeed opens up a fertile platform to realize a new class of higher-order mode conversion device which would be suitable for various optical pumping scheme through higher-order modes, high-power delivery through higher-order modes, and may also open up future platform towards mode-multiplexing processes. Moreover, in the presence of nonlinearities, the proposed EP4-aided successive state conversion scheme can potentially be explored to design all-optical circulators and isolators for state-of-the-art integrated (on-chip) photonic circuits for future communication systems and signal processing. The experimental realization of EP4-aided state dynamics would be feasible by exploiting the proposed scheme in any suitable guided-wave system. The proposed design philosophy along with the customized optical system will certainly open up an avenue to host EPs of the order of more than four, such as EP5 and EP6.

V. SUMMARY

In summary, we have reported a configuration of a simple fabrication feasible gain-loss-assisted Fabry-Pérot type trilayer optical microcavity to host EPs up to order four. Estimating the cavity states in terms of the S-matrix poles, we have chosen to study the simultaneous interactions among four cavity states with an appropriate modulation of an unbalanced gain-loss profile. We have encountered three connecting EP2s among four coupled states by tuning the gain-loss profile of a thin (in comparison to the total microcavity length) bilayer at both sides of the microcavity based on only two coupling control parameters. Now, encircling at least two connecting EP2s (among three) inside a closed contour in the gain-loss plane, we have achieved the functionality of a cube-root branch point with encounter of an EP3, and accordingly we have embedded a total of three EP3s in the system's parameter space. Furthermore, we have exclusively

reported the hosting of an EP4 by enclosing all the three connecting EP2s inside a gain-loss parameter space. Besides the verification of second-order and third-order branch-point behaviors of embedded EP2s and EP3s in terms of adiabatic state-flipping applications between two states, and successive state-switching applications among three states, respectively, we have established an exclusive EP4-aided topological state-switching phenomena among four coupled states in a row. Thus, a specific design of a real optical system hosting an EP4 has exclusively been reported, where in addition to EP4, one can host multiple connecting EP2s and EP3s. Besides the strong impact in the fundamental physics of EP singulari-

ties, the proposed cavity configuration along with the scheme of the hosting of different orders of EPs has a potential to boost the technologies for growth of advanced optical elements for high-performance integrated (or on-chip) devices.

ACKNOWLEDGMENTS

[1] B. Midya, H. Zhao, and L. Feng, Nat. Commun. **9**, 2674 (2018).

[2] M.-A. Miri and A. Alù, Science **363**, eaar7709 (2019).

[3] Ş. K. Özdemir, S. Rotter, F. Nori, and L. Yang, Nat. Mater. **18**, 783 (2019).

[4] T. Kato, *Perturbation Theory for Linear Operators* (Springer, Berlin, 1966).

[5] W. D. Heiss, Phys. Rev. E **61**, 929 (2000).

[6] W. D. Heiss, J. Phys. A: Math. Theor. **45**, 444016 (2012).

[7] H. Eleuch and I. Rotter, Phys. Rev. A **93**, 042116 (2016).

[8] M. Müller and I. Rotter, J. Phys. A: Math. Theor. **41**, 244018 (2008).

[9] W. D. Heiss, J. Phys. A: Math. Theor. **41**, 244010 (2008).

[10] G. Demange and E.-M. Graefe, J. Phys. A: Math. Theor. **45**, 025303 (2011).

[11] W. D. Heiss and G. Wunner, J. Phys. A: Math. Theor. **49**, 495303 (2016).

[12] H. Eleuch and I. Rotter, Eur. Phys. J. D **69**, 229 (2015).

[13] H. Eleuch and I. Rotter, Eur. Phys. J. D **69**, 230 (2015).

[14] J.-W. Ryu, S.-Y. Lee, and S. W. Kim, Phys. Rev. A **85**, 042101 (2012).

[15] S. Bhattacherjee, A. Laha, and S. Ghosh, Phys. Scr. **94**, 085202 (2019).

[16] J. Doppler, A. A. Mailybaev, J. Böhm, U. Kuhl, A. Girschik, F. Libisch, T. J. Milburn, P. Rabl, N. Moiseyev, and S. Rotter, Nature (London) **537**, 76 (2016).

[17] X.-L. Zhang, S. Wang, B. Hou, and C. T. Chan, Phys. Rev. X **8**, 021066 (2018).

[18] J. Schnabel, H. Cartarius, J. Main, G. Wunner, and W. D. Heiss, Phys. Rev. A **95**, 053868 (2017).

[19] X.-L. Zhang and C. T. Chan, Commun. Phys. **2**, 63 (2019).

[20] H. K. Gandhi, A. Laha, S. Dey, and S. Ghosh, Opt. Lett. **45**, 1439 (2020).

[21] S. Dey, A. Laha, and S. Ghosh, Phys. Rev. B **101**, 125432 (2020).

[22] S. N. Ghosh and Y. D. Chong, Sci. Rep. **6**, 19837 (2016).

[23] A. Laha, A. Biswas, and S. Ghosh, Phys. Rev. Appl. **10**, 054008 (2018).

[24] A. Laha, A. Biswas, and S. Ghosh, J. Opt. Soc. Am. B **34**, 2050 (2017).

[25] A. Laha, A. Biswas, and S. Ghosh, J. Opt. **21**, 025201 (2019).

[26] A. Laha, D. Beniwal, S. Dey, A. Biswas, and S. Ghosh, Phys. Rev. A **101**, 063829 (2020).

[27] J. Kullig, C.-H. Yi, M. Hentschel, and J. Wiersig, New J. Phys. **20**, 083016 (2018).

[28] K. Ding, Z. Q. Zhang, and C. T. Chan, Phys. Rev. B **92**, 235310 (2015).

[29] D. A. Bykov and L. L. Doskolovich, Phys. Rev. A **97**, 013846 (2018).

[30] M. Liertzer, L. Ge, A. Cerjan, A. D. Stone, H. E. Türeci, and S. Rotter, Phys. Rev. Lett. **108**, 173901 (2012).

[31] H. Hodaei, A. U. Hassan, W. E. Hayenga, M. A. Miri, D. N. Christodoulides, and M. Khajavikhan, Opt. Lett. **41**, 3049 (2016).

[32] B. Peng, Ş. K. Özdemir, M. Liertzer, W. Chen, J. Kramer, H. Yılmaz, J. Wiersig, S. Rotter, and L. Yang, Proc. Natl. Acad. Sci. USA **113**, 6845 (2016).

[33] H. Cartarius, J. Main, and G. Wunner, Phys. Rev. Lett. **99**, 173003 (2007).

[34] H. Menke, M. Klett, H. Cartarius, J. Main, and G. Wunner, Phys. Rev. A **93**, 013401 (2016).

[35] R. Lefebvre, O. Atabek, M. Šindelka, and N. Moiseyev, Phys. Rev. Lett. **103**, 123003 (2009).

[36] C. Dembowski, H.-D. Gräf, H. L. Harney, A. Heine, W. D. Heiss, H. Rehfeld, and A. Richter, Phys. Rev. Lett. **86**, 787 (2001).

[37] C. Dembowski, B. Dietz, H.-D. Gräf, H. L. Harney, A. Heine, W. D. Heiss, and A. Richter, Phys. Rev. Lett. **90**, 034101 (2003).

[38] C. Dembowski, B. Dietz, H.-D. Gräf, H. L. Harney, A. Heine, W. D. Heiss, and A. Richter, Phys. Rev. E **69**, 056216 (2004).

[39] R. Gutöhrlein, J. Main, H. Cartarius, and G. Wunner, J. Phys. A: Math. Theor. **46**, 305001 (2013).

[40] R. Gutöhrlein, H. Cartarius, J. Main, and G. Wunner, J. Phys. A: Math. Theor. **49**, 485301 (2016).

[41] E. M. Graefe, U. Günther, H. J. Korsch, and A. E. Niederle, J. Phys. A: Math. Theor. **41**, 255206 (2008).

[42] H. Xu, D. Mason, L. Jiang, and J. G. E. Harris, Nature (London) **537**, 80 (2016).

[43] H. Jing, Ş. K. Özdemir, H. Lü, and F. Nori, Sci. Rep. **7**, 3386 (2017).

[44] A. Ben-Asher, D. Šimsa, T. Uhlířová, M. Šindelka, and N. Moiseyev, Phys. Rev. Lett. **124**, 253202 (2020).

[45] A. A. Zyablovsky, E. S. Andrianov, and A. A. Pukhov, Sci. Rep. **6**, 29709 (2016).

[46] X. Yin and X. Zhang, Nat. Mater. **12**, 175 (2013).

[47] R. Thomas, H. Li, F. M. Ellis, and T. Kottos, Phys. Rev. A **94**, 043829 (2016).

[48] Y. Choi, C. Hahn, J. W. Yoon, S. H. Song, and P. Berini, Nat. Commun. **8**, 14154 (2017).

[49] A. Laha, S. Dey, H. K. Gandhi, A. Biswas, and S. Ghosh, ACS Photonics **7**, 967 (2020).

[50] T. Goldzak, A. A. Mailybaev, and N. Moiseyev, Phys. Rev. Lett. **120**, 013901 (2018).

[51] J. Wiersig, Phys. Rev. A **93**, 033809 (2016).

[52] H. Hodaei, A. U. Hassan, S. Wittek, H. Garcia-Gracia, R. El-Ganainy, D. N. Christodoulides, and M. Khajavikhan, Nature (London) **548**, 187 (2017).

[53] W. Chen, Ş. Kaya Özdemir, G. Zhao, J. Wiersig, and L. Yang, Nature (London) **548**, 192 (2017).

[54] C. Zeng, Y. Sun, G. Li, Y. Li, H. Jiang, Y. Yang, and H. Chen, Opt. Express **27**, 27562 (2019).

[55] I. Gilary, A. A. Mailybaev, and N. Moiseyev, Phys. Rev. A **88**, 010102(R) (2013).

[56] T. J. Milburn, J. Doppler, C. A. Holmes, S. Portolan, S. Rotter, and P. Rabl, Phys. Rev. A **92**, 052124 (2015).

[57] K. Ding, G. Ma, M. Xiao, Z. Q. Zhang, and C. T. Chan, Phys. Rev. X **6**, 021007 (2016).

[58] X. Zhou, S. K. Gupta, Z. Huang, Z. Yan, P. Zhan, Z. Chen, M. Lu, and Z. Wang, App. Phys. Lett. **113**, 101108 (2018).

[59] J. Jia, B. Zhu, F. Ye, H. Zhong, and H. Deng, Euro. Phys. J. D **74**, 117 (2020).

[60] S. Bhattacherjee, H. K. Gandhi, A. Laha, and S. Ghosh, Phys. Rev. A **100**, 062124 (2019).

[61] D. A. Bykov and L. L. Doskolovich, J. Light. Technol. **31**, 793 (2013).

[62] L. Ge, Y. D. Chong, S. Rotter, H. E. Türeci, and A. D. Stone, Phys. Rev. A **84**, 023820 (2011).